# Extensive Validation of Computed Laminar Flow in a Stirred Tank with Three Rushton Turbines

**J. M. Zalc, M. M. Alvarez, and F. J. Muzzio**
Dept. of Chemical and Biochemical Engineering, Rutgers University, P.O. Box 909, Piscataway, NJ 08855

**B. E. Arik**
Dantec Dynamics, Mahwah, NJ 07430

*High-resolution CFD results, supplemented by extensive experimental validation, are presented for Newtonian laminar flow fields in a stirred tank equipped with three Rushton turbines. Flow fields are computed using the ORCA software suite for Reynolds numbers ranging from 20 to 200 with an unstructured tetrahedral mesh containing roughly 2 million tetrahedra. Each of the flow solutions takes less than 8 h to converge when running in parallel on eight desktop workstations. Excellent agreement is obtained between computed velocity fields and planar velocity vectors obtained using particle image velocimetry. Planar laser-induced fluorescence was used to expose persistent poor-mixing regions, in excellent agreement with numerical results. The computational results used illustrate strong flow compartmentalization and significant spatial heterogeneity with respect to local deformation rates within the vessel.*

## Introduction

Stirred tanks are widely used in the chemical processing industries for blending (Godfrey, 1992), liquid–liquid dispersion (Wichterle, 1995), gas–liquid dispersion (Hudcova et al., 1989), suspension formation (Saravanan et al., 1997) heat transfer (Xu et al., 1997), mass transfer (Montes et al., 1999), and reactions (Ali and Menzinger, 1997; Bourne and Yu, 1994). Efficient mixing is crucial to the outcome of all of these processes. Poor mixing can have a negative impact, such as inconsistent product quality in blended products, excessive byproduct formation in cases involving multiple reactions (Zalc and Muzzio, 1999), wide particle-size distributions in crystallization processes, and slow mass-transfer rates in bioreactors and multiphase reactors. Turbulent flows are often used to achieve high mixing rates, but there are many instances in which working in the laminar regime is unavoidable. For instance, turbulence is practically unattainable when blending viscous doughs or pastes. Turbulence is undesirable in fermentors where the high shear rates and random velocity fluctuations associated with turbulence can lead to excessive rates of cell damage and death (Cherry and Papoutsakis, 1988; Croughan et al., 1987). Surprisingly, few data exist regarding flow and mixing in stirred-tank reactors in the laminar regime.

Early experimental work on stirred tanks yielded gross measurement of power requirements at different agitation rates (Aiba, 1958; O'Connell and Mack, 1950). Studies reporting power requirements of stirred tanks tacitly expected that the more energy drawn from the impeller, the better the mixing, assuming that energy would be dissipated uniformly and effectively. Experimental techniques developed later for investigating flow systems locally were intrusive in nature. The insertion of probes into the flow was used to determine velocity components and illustrate bulk-flow patterns (Desouza and Pike, 1972; Norwood and Metzner, 1960). Unfortunately, only a small number of such probes could be used, because the presence of the probes extensively perturbed the flow of interest. Mixing times have been studied based on conductivity or pH measurements using several probes inserted into the flow (Biggs, 1963; Hayes et al., 1998; Jahoda and Machon, 1994). The results obtained depend strongly on the number and location of the probes.

---

Correspondence concerning this article should be addressed to F. J. Muzzio.

More recently, experimental techniques have been developed to obtain nonintrusive measurements of flow variables. One group (Holden et al., 1998) has applied electrical resistance tomography to measure nonintrusively time-resolved concentrations at a spatial resolution of $O(10^4)$ points within a tank and to estimate mixing rates. Other researchers (Distelhoff et al., 1997) have used laser-induced fluorescence to measure nonintrusively scalar concentration profiles. Also, particle image velocimetry (PIV) has been used to determine planar velocity measurements for $O(10^3)$ points within the flow (LaFontaine and Shepherd, 1996). However, PIV is a visual technique that can be difficult to apply to systems with complex geometries. Even with all of these experimental techniques, it would be very time-consuming and costly to evaluate in detail a large number of system geometries and/or flow conditions.

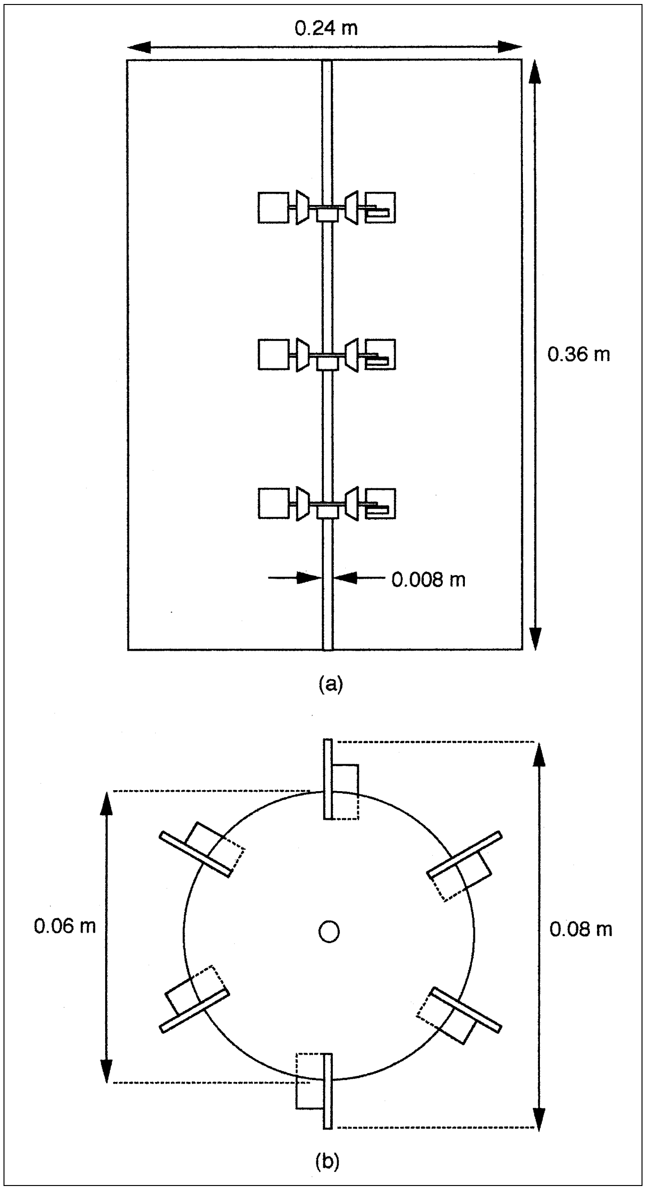

**Figure 1. Three-Rushton-turbine stirred-tank system.**

Some computational work has been done on industrial mixing devices, although many of the studies have relied on assumptions that are not physically justifiable. One researcher (Smith, 1997) has attempted to study flow and mixing in a stirred tank by solving for an azimuthally symmetric flow. Several groups (Harvey and Rogers, 1996; Ranade, 1997) have performed computational fluid dynamics analysis of baffled stirred tanks by computing a pseudosteady state solution that is really an instantaneous snapshot of a time-dependent three-dimensional (3-D) flow. In such a case, circumferentially averaged simulation results were compared with experimental data. This approach can be useful for visualizing bulk-flow patterns, but is unacceptable for conducting a complete mixing study. Other workers have exploited the symmetry of the Rushton turbine (Lamberto et al., 1999) and pitched-blade turbine (Bakker et al., 1996) geometries to solve for the flow field in one-sixth and one-quarter, respectively, of the stirred tanks of interest. However, such symmetry will not exist in all cases, especially if geometric variations are added in an effort to improve mixing performance, or if the flow exhibits slow oscillatory behavior with a different spatial symmetry. To the best of our knowledge, only one group (Harvey et al., 2000) has solved the full laminar flow fields in unbaffled stirred tanks with multiple impellers. Their work focused on using the flow fields to generate a particle-mapping algorithm to predict isolated mixing regions; a detailed analysis of the flow characteristics was not presented.

This article introduces efficient computational tools for obtaining high-resolution numerical results for laminar flow in stirred tanks. The tools are of enough accuracy that mixing dynamics and patterns such as the structure of persistent poor-mixing regions can be investigated with unprecedented detail in a stirred tank equipped with three Rushton turbines. Extensive comparison with experimental PIV and planar laser-induced fluorescence (PLIF) results is also presented. This validation serves as a foundation for future contributions focused on quantifying mixing performance in this and other devices. The following section presents a detailed explanation of the mixing device studied and the computational methods used. Results are given in the third section, and conclusions of this work are presented in the final section.

## System Geometry and Computational Techniques

The system under investigation in this article is a stirred tank equipped with three six-bladed Rushton turbines (shown in Figures 1a and 1b). The tank itself is a vertical, cylindrical vessel with a diameter of 0.24 m and a height-to-diameter ratio of 1.5. Since only laminar flow will be considered in this work, an unbaffled tank is chosen; baffles are generally used to inhibit vortex formation under turbulent operation and are widely known to be detrimental to mixing performance in the laminar regime. Further, the existence of baffles would preclude steady flow in any reference frame due to the relative motion between the impeller blades and the baffles. This complexity would dramatically increase the computational effort needed to solve the velocity and pressure fields.

The concentrically located shaft extends the entire height of the vessel and has a diameter of 0.008 m. The disks, blades, and supports are all 0.001 m thick. The three impellers are equally spaced in the vertical direction, and the tip-to-tip impeller diameter, $D_I$, is 0.08 m, while the diameter of the disks on which the blades are mounted is 0.06 m. The six blades on each impeller are spaced at 60° increments and the face of each blade is 0.015 m by 0.015 m. It should be noted that the computational model of this system represents the geometry exactly; even the small, angled supports that prevent each impeller blade from shifting are modeled.

The working fluid in the experimental system is a water/glycerine solution, which has a viscosity, $\mu$, of 0.4 kg/(m·s) and a density, $\rho$, of 1.247 kg/(m$^3$). The flow condition is represented by the Reynolds number, *Re*, which, as is customary, is computed according to Eq. 1:

$$Re = \frac{\rho N D_I^2}{\mu}. \tag{1}$$

For $Re = 20.0$, $N$ is 1.0 rps. The other Reynolds numbers are simulated by changing the agitation rate. Reynolds numbers of 20, 40, 60, 80, 100, 120, 140, 160, 180, and 200 are simulated.

For the computations presented in this work, ORCA (Fujitsu, Campbell, CA) was used. The ORCA package includes tools for parametric geometry definition, unstructured tetrahedral meshing, flow-field solution, and Eulerian and Lagrangian postprocessing routines. The computational mesh for our system geometry contains 370,340 nodes forming 1,944,799 first-order tetrahedral elements, with individual cell sizes ranging from $5.61 \cdot 10^{-12}$ m$^3$ to $2.93 \cdot 10^{-7}$ m$^3$. Edge lengths of individual tetrahedra range from $1.77 \cdot 10^{-4}$ to $1.52 \cdot 10^{-2}$, with aspect ratios ranging from 1.00 to 5.57, with an average of 1.48, and a standard deviation of 0.42. Once the discretization of the flow domain has been performed, the CFD solver is used to obtain approximate values for the velocity components and pressure at each of the node points. The specific solver is acuSolve (ACUSIM Software, Saratoga, CA), which uses a full finite-element formulation to solve the fully coupled mass and momentum conservation equations. The flow is incompressible, and Eq. 2 shows the momentum conservation in the rotation frame:

$$\rho \frac{D\boldsymbol{v}_{rf}}{Dt} + 2\boldsymbol{\Omega} \times \boldsymbol{r} + \boldsymbol{\Omega} \times \boldsymbol{\Omega} \times \boldsymbol{r} = -\nabla p - \nabla \cdot \bar{\boldsymbol{\tau}} + \rho \boldsymbol{g}, \tag{2}$$

where, $\bar{\boldsymbol{\tau}}$ is the shear stress tensor; $p$ is the pressure; $\boldsymbol{g}$ is the gravitational force vector, $\boldsymbol{r}$ is the radial position vector extending from the tank axis to a point in the flow domain; $\boldsymbol{\Omega}$ is the angular velocity vector ($\boldsymbol{\Omega} = \{0, 2\pi N \text{ (rad/s)}, 0\}$); and $N$ is the number of revolutions per second. It should be noted that the coriolis and centrifugal terms exist because this equation has been expressed in a reference frame rotating with the impellers. As demonstrated by experiments, the rotating-frame velocity field, $\boldsymbol{v}_{rf}$, is time-independent for the Reynolds numbers considered here, and is related to the stationary frame velocity field, $\boldsymbol{v}$, by Eq. 3:

$$\boldsymbol{v} = \boldsymbol{v}_{rf} + \boldsymbol{\Omega} \times \boldsymbol{r}. \tag{3}$$

Further, mass conservation dictates that the computed velocity field be divergence-free, regardless of the reference frame. This condition is mathematically given by Eq. 4:

$$\nabla \cdot \boldsymbol{v}_{rf} = \nabla \cdot \boldsymbol{v} = 0. \tag{4}$$

The velocity boundary conditions for all nodes on the impellers and shaft are set to zero. In all cases, the top surface of the tank is assumed to be flat and a zero shear-stress boundary condition is set for all nodes along that surface. It should be noted that the assumption of a flat upper surface is well justified, because significant vortexing does not occur for the flow conditions considered in this work (Rushton et al., 1950). The velocity boundary conditions for the nodes on the cylindrical vessel surface and the bottom are set to correspond to the solid-body rotation. Also, the fluid-node velocities are initially assumed to correspond to the same solid-body rotation as the tank walls.

In each simulation, the solution is taken to be converged when the normalized residuals for the three velocity components and the pressure all fall below $10^{-4}$. The computations are run in parallel on eight HAL class 375 machines (Fujitsu, Campbell, CA), where the calculation of the velocity and pressure fields for each Reynolds number takes between 75 and 200 iterations to converge, and each run takes less than 8 h of CPU time on each of the eight processors. The speed of these calculations means that the laminar flow field in a stirred tank can be computed for a two-million-element mesh during the course of a working day. Even fairly recently (Lamberto et al., 1999) similar computations for smaller meshes took several weeks of CPU time on computers of comparable cost.

As amply demonstrated by experience, CFD results should be validated by experimental data. Computational results depend strongly on proper geometric definition, suitable discretization of the flow domain, setting of boundary conditions, convergence criteria, algebraic implementation of the properly discretized form of the governing equations, among others. A CFD solution can converge well and the resulting flow field can appear reasonable at first; however, significant flow features may be absent due to insufficient mesh resolution in a particular portion of the flow domain. Mixing studies, in particular, require extensive validation because, as is well known in the literature of chaotic flows, small errors ("perturbations") in the flow can cause huge changes in mixing performance (Alvarez et al., 2000). Validation of the current work is two-pronged. First, computed bulk-flow patterns in a vertical plane cutting through the tank are compared with results obtained via particle-image velocimetry. The PIV apparatus (Dantec, Mahwah, NJ), which is shown in Figure 2, is used to measure planar velocity components for vertical planes in the stirred vessel at different Reynolds numbers. In the PIV experiments, the glycerin is seeded with 5 $\mu$m, silver-coated, hollow glass beads at a density of 10 mg per liter of solution. The particles are small, neutrally buoyant, and follow the flow field closely. A laser light sheet is passed through the transparent experimental apparatus, and a digital camera is used to capture images of the illuminated plane. In such images, the particles located in that plane appear as bright points in a dark background. Two successive snapshots of the illuminated plane are required in order to calculate the planar velocity field using a cross-correlation algorithm, which identifies pairs of particles present in both snapshots and computes the velocities based on the displacement of each particle and the elapsed time between successive frames. The Dantec PIV equipment includes software (Flow Manager 2.1) that performs the cross-correlation analysis and averaging.

In addition, mixing patterns and details of segregated regions are revealed using PLIF, an illumination technique in which mixing structures along two-dimensional planes within the stirred vessel are exposed. The experimental system is illuminated with a YAG laser sheet (1-mm thickness; wavelength = 535 nm) in an otherwise dark room. The mixing structure of the illuminated 2-D plane is revealed when injecting a fluorescent tracer, which is rhodamine G dissolved in glycerin. Rhodamine G serves as a passive tracer once its buoyancy has been properly matched with the bulk fluid in the tank. Images of the illuminated plane are captured in 35-mm slide film using a photographic camera, as shown in Figure 2.

## Results

### *Computational and experimental velocity fields*

In order to illustrate the agreement between CFD results and experimental measurements regarding bulk flow patterns in the stirred tank, planar velocity vectors are compared for a vertical plane aligned with one of the impeller blades. Figures 3a–3d show comparisons of CFD and PIV results for *Re* = 20, 40, 80, and 160, respectively. Velocity vectors in the left half of each figure are interpolated based on CFD solutions for the flow fields. The velocity components are interpolated for a lattice of 30 (radial)×90 (vertical) spatial locations covering half of the vessel cross-section. All of the vectors are shown with the same length, and the color-coding is based on the planar velocity magnitude normalized with respect to the tip speed of the impeller. The vectors in the right half of each figure are the corresponding PIV results for the planar velocities. In Figure 3a, both the computational and experimental results indicate that six recirculation loops exist, with one located above and one located below each impeller. For *Re* = 20, the maximum velocity magnitude in this vertical plane is only 20% of the tip speed of the impeller, indicating that the flows associated with the recirculation regions are relatively weak for this flow condition. Excellent agreement is obtained between the computational and experimental results with regard to the locations of the centers of these recirculation regions. Because these flow patterns only represent a single vertical plane in a fully 3-D flow, it is impossible to conclude that segregated regions do indeed exist until Lagrangian analysis is performed. Results of such analysis are presented in a later section. Figure 3b shows results for *Re* = 40. The flow patterns are substantially different from those presented in Figure 3a. For *Re* = 40, the planar velocity magnitudes reach 32% of the impeller tip speed, as opposed to 20% for *Re* = 20. Again, good agreement regarding velocity directions and magnitudes is obtained between the CFD and PIV results. The third flow condition for which validation of the flow patterns is performed is *Re* = 80, as shown in Figure 3c. Here, four recirculation regions are apparent, with the centers of two located below and above the upper and lower impeller blades, respectively, and the centers of the other two located near the midheight of the vessel and close to the wall. For this flow condition, the planar velocity magnitudes reach 52% of the tip speed of the impeller and reasonable agreement is obtained between the computational and experimental results. Figure 3d shows flow patterns from CFD results without the corresponding experimental results. Here, the planar velocity magnitudes reach 52% of the tip speed of the impeller and the flow patterns are similar to those for *Re* = 80 (cf. Figure 3c). The observations concerning the maximum percentage of the impeller tip speed that is attained by the planar velocity magnitudes reveal that at the lower Reynolds numbers considered in this work, the flow within the recirculation regions is relatively weak and the dominant flow is azimuthal. At the higher Reynolds numbers, inertial effects become more significant and the relative strength of the recirculation regions becomes greater. Both the experiments and the computations reveal significant differences in flow stuctures as a function of agitation rate. Lagrangian techniques are used next to investigate asymptotic mixing behavior with this stirred-tank system.

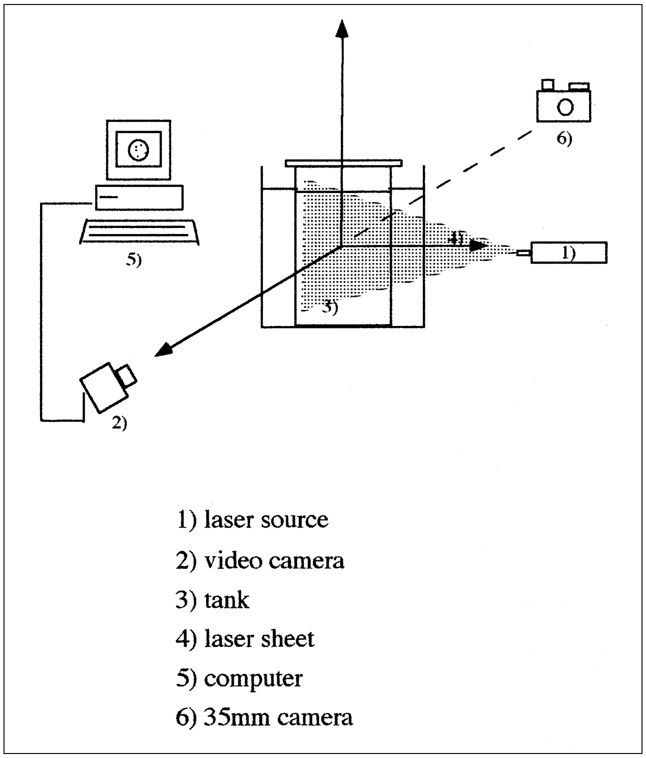

**Figure 2. PIV/LIF equipment.**

A more quantitative comparison method for comparing the numerical and experimental results for the flow fields is to plot profiles of velocity components along a line. Consider a vertical line situated halfway to the tank wall, aligned with one of the impeller blades and extending the entire height of the vessel. The velocity components along this line can be interpolated using the CFD results and compared with PIV data, as shown in Figures 4aa–4c. In each case, the horizontal axis represents the vertical distance along the line and the

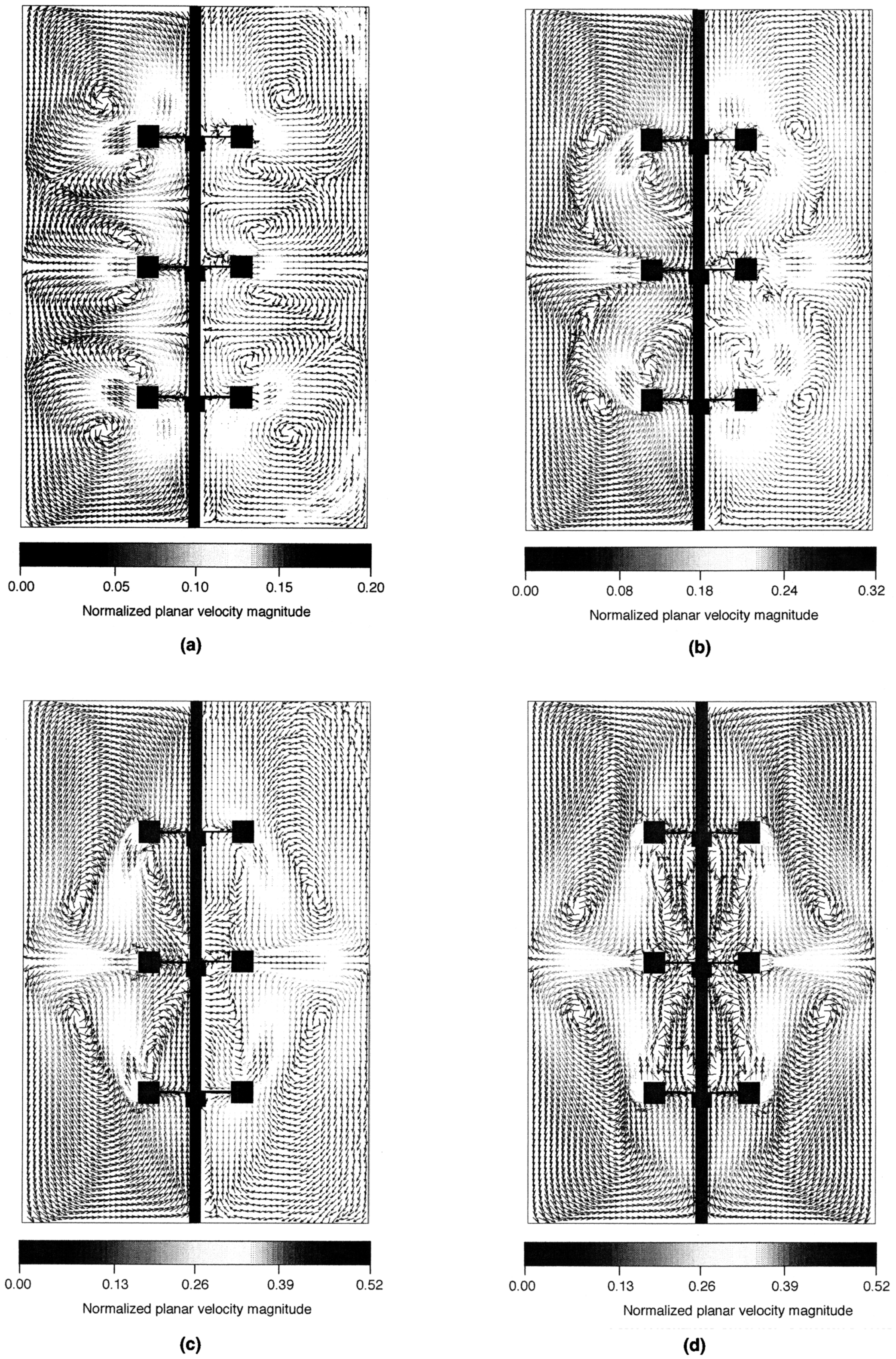

**Figure 3. CFD and experimental results for flow patterns in a vertical plane cutting through the center of the tank and aligned with an impeller blade.**

For (a) $Re = 20$, (b) $Re = 40$, (c) $Re = 80$, (d) $Re = 160$.

vertical axis represents the vertical and radial velocity components normalized with respect to the impeller tip speed. CFD results are shown as thin lines (normalized vertical velocity) and thick lines (normalized radial velocities). PIV data are shown as circles (normalized vertical velocity) and squares (normalized radial velocities). Results for *Re* = 20 are shown in Figure 4a. Excellent agreement is attained between the experimental and computational results. Three local maxima exist for the normalized radial velocity and the values at these maxima are very similar, with the middle peak being slightly lower than the other two. As expected, these maxima exist at vertical heights corresponding to the positions of the three impellers. The profiles are quite symmetric about the mid-height of the vessel ($y = 0.18$ m) although the boundary conditions are not the same at the top and bottom of the tank. The normalized vertical velocities are of smaller magnitude than the radial velocities. In Figure 4b, results are shown for *Re* = 40. Once again, excellent agreement exists between the numerical and experimental results. Three maxima exist for the normalized radial velocity with the middle peak being significantly larger than the other two. The magnitudes of the normalized vertical velocities are larger than for *Re* = 20 (cf. Figure 4a). A larger positive peak exists at a height of approximately 0.12 m, while a large negative peak exists at roughly 0.24 m. The results for *Re* = 80 are shown in Figure 4c, and large differences exist for this flow condition. Now, a single large peak in the normalized radial velocity exists at 0.18 m, indicating that for this flow condition, inertial effects are significant and the flow is dominated by the outward ejection of fluid by the middle impeller. One large positive peak in normalized vertical velocity exists near a height of 0.12 m and a large negative peak in normalized vertical velocity exists near a height of 0.21 m. Overall, these results indicate that as the agitation rate is increased within this range, the outward radial flow associated with the middle impeller becomes more and more dominant. In addition, the normalized vertical velocities become increasingly dominant because the fluid that is ejected outward radially by the middle im-

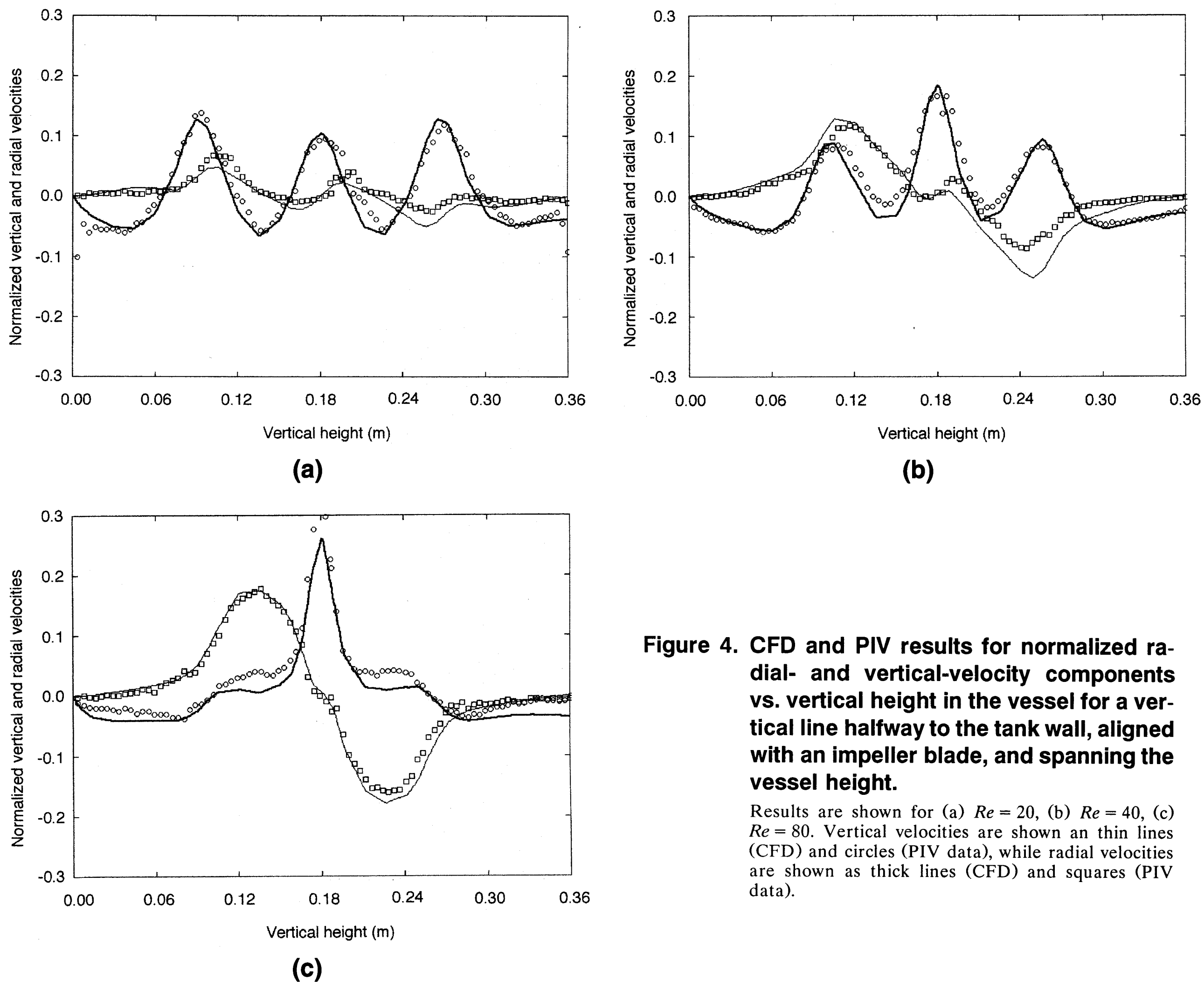

**Figure 4. CFD and PIV results for normalized radial- and vertical-velocity components vs. vertical height in the vessel for a vertical line halfway to the tank wall, aligned with an impeller blade, and spanning the vessel height.**

Results are shown for (a) *Re* = 20, (b) *Re* = 40, (c) *Re* = 80. Vertical velocities are shown an thin lines (CFD) and circles (PIV data), while radial velocities are shown as thick lines (CFD) and squares (PIV data).

peller must recirculate through the impeller regions. The results of Figure 4 show that excellent quantitative agreement exists between the computed and measured flow fields in the stirred tank. This validation work is a vital part of our investigation, but the flow fields themselves provide no information about mixing performance, which will be addressed next.

### *Chaotic and regular mixing regions*

A common approach to understand complex chaotic phenomena in periodic spatiotemporal domains is to reduce the number of dimensions by exploring time-discrete dynamics. By considering stroboscopic snapshots of particle trajectories and plotting all of the intersections on a single graph, a Poincaré section is computed, revealing asymptotic mixing behavior. In the case of the stirred tank, consider the rotating frame velocity field in which the impellers remain still while the tank is spun. A lattice of 16 (radial) by 48 (vertical) particles is initially aligned with one of the impeller blades and covers half of the vertical cross section of the stirred tank. This initial configuration was chosen so that particles exist both inside and outside islands for all flow conditions investigated. Otherwise, the resulting Poincaré section would possess large empty regions indicative of poor-mixing regions, but no structural details whatsoever would be evident. The intersection surface chosen is a vertical plane extending from the shaft to the tank wall and aligned with one of the impeller blades. Particle trajectories are computed for 600 tank rotations and the position is recorded every time a particle crosses the intersection surface. All of the intersections are plotted on one graph and chaotic and regular regions are exposed. Chaotic regions appear as random-like clouds of points in a Poincaré section, and regular regions manifest themselves as regions devoid of points or as closed loops.

The bottom half of Figure 5a shows the Poincaré section computed for $Re = 20$. The top half of this figure shows a PLIF image after several hours for an injection initially located in the chaotic region. Just as six recirculation loops were visible in the results of Figure 3a, the Lagrangian results indicate that, indeed, six regions of regular flow exist. The sizes and locations of segregated poor-mixing regions are very similar in the Poincaré section and the experimental PLIF results. It should be noted that in the experimental image, no details within the islands of regular flow can be seen because the rhodamine was initially injected into the chaotic region and can only enter the islands by diffusion after extremely long times. In any event, both the computations and the experimental results reveal that segregated regions exist in this

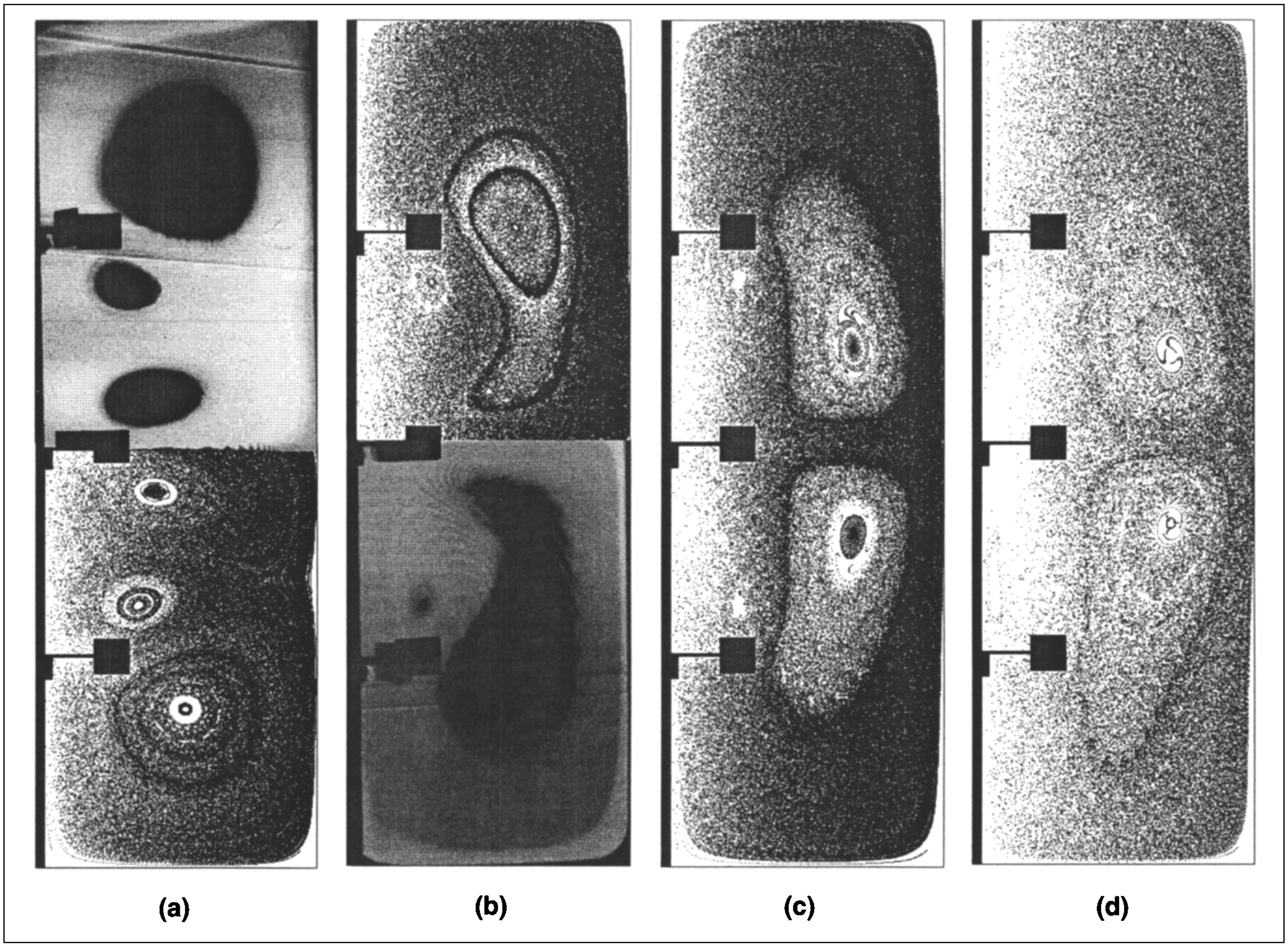

**Figure 5. Poincaré sections for (a) $Re = 20$, (b) $Re = 40$, (c) $Re = 80$, (d) $Re = 160$.**

system at $Re = 20$. Similar results are shown for $Re = 40$ in Figure 5b. In this case, the top half of the figure shows the computed Poincaré section, while the PLIF results are in the lower half. Again, remarkable agreement between simulations and experiments concerning the sizes and locations of segregated regions is achieved. In this case, two small islands are evident, one near the top impeller and one near the bottom impeller. In addition, there are two large kidney-bean-shaped islands outward radially from the impeller assembly. Figures 5c and 5d present Poincaré sections for $Re = 80$ and $Re = 160$, respectively. Corresponding experimental images are not shown for these two flow conditions because excessive vibrations existed in the experimental system at these higher agitation rates and caused rapid destruction of the poor-mixing islands. The use of a less viscous water/glycerine solution and lower agitation rates to achieve $Re = 80$ and $Re = 160$ would have resulted in excessive diffusivity that would have similarly eliminated the poor-mixing regions that are revealed by the simulations. The Poincaré sections for these two cases do not differ greatly. However, the $Re = 80$ case exhibits two small islands, one directly above the lowest impeller blade and one below the highest impeller blade. The two small islands do not exist in these locations in the $Re = 160$ case, instead they are located near the shaft. Also, the two larger islands in the $Re = 160$ case have moved outward radially and closer to the midheight of the vessel when compared to the results for the $Re = 80$ case. All of these results indicate that large differences in flow fields and mixing behavior exist over a relatively small range of Reynolds numbers in the laminar regime for the three-Rushton-turbine stirred tank and that these differences are robustly captured by our numerical simulations and corresponding experimental investigations. However, the differences in mixing behavior addressed in this work are qualitative in terms of sizes and shapes of regular poor-mixing islands; a comprehensive quantitative analysis of mixing in this device will be relayed in a future communication.

### *Circulation*

The flow in the three-Rushton-turbine stirred tank possesses separatrices that forbid the convective passage of material. Consequently, the flow is strongly compartmentalized. Workers have attempted to model mixing in such geometries by imaging a series of well-mixed compartments that communicate weakly with each other (Ando et al., 1990; Cui et al., 1996). In order to quantify vertical flows in our stirred-tank system, velocity components were interpolated at approximately 75,000 equally spaced locations on each of 35 horizontal cross sections of the vessel for each of the Reynolds numbers studied. The planes are equally spaced in the vertical direction and span the entire vessel. The circulation velocity, *Q*, is computed as one half of the mean of the absolute values of the vertical velocity components interpolated at the $\approx$ 75,000 points along each cross section.

Figure 6 illustrates differences in *Q/Re* as a function of vertical height within the vessel for different Reynolds numbers. Recall that $y = 0$ m and $y = 0.36$ m correspond to the bottom and top of the vessel, respectively. Also, the lower, middle, and upper impellers are located at heights of $y = 0.09$ m, $y = 0.18$ m, and $y = 0.27$ m, respectively. *Q/Re* must be identically zero at $y = 0$ m and $y = 0.36$ m because the vessel is a batch system and no fluid can traverse the horizontal cross sections at these locations. For all of the Reynolds numbers investigated here, the absolute minimum of *Q/Re* for the internal planes exists at the midheight of the tank ($y = 0.18$ m), but is not identically zero there. Values of *Q/Re* at $y = 0.18$ m range from $2.9 \cdot 10^{-7}$ m/s for $Re = 20$ to $5.5 \cdot 10^{-5}$ m/s for $Re = 200$. If the tank were to have a fixed lid on it, then the boundary conditions, in addition to the system geometry, would be symmetric about the midheight of the vessel and the vertical communication would be zero along the plane at $y = 0.18$ m. Recall that a zero shear stress exists for the upper surface of our vessel, so the asymmetry of the boundary conditions is what allows the finite vertical communication (albeit small) to exist at the midheight of the vessel for the Reynolds numbers considered in this work. These ideas would lead one to believe that introducing asymmetry into the system geometry would enhance vertical mixing in this device.

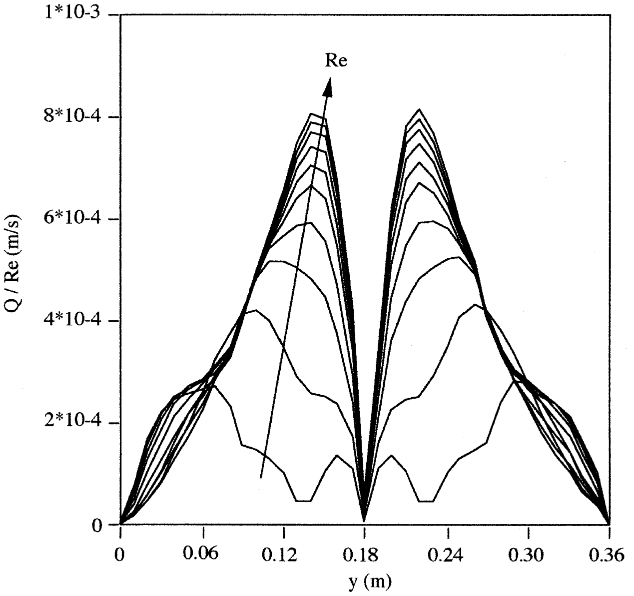

**Figure 6. *Q/Re* vs. vertical height in the tank for *Re* = 20, 40, 60, 80, 100, 120, 140, 160, 180, and 200.**

For all of the curves shown in Figure 6, significant heterogeneity of *Q/Re* exists with respect to vertical height in the tank. At $Re = 20$, local maxima of *Q/Re* exist near $y = 0.07$ m, $y = 0.16$ m, $y = 0.20$ m, and $y = 0.29$ m. The value of $2.8 \cdot 10^{-4}$ m/s at $y = 0.29$ m represents the global maximum for $Re = 20$, while the value of *Q/Re* at $y = 0.07$ m is slightly lower and is $2.7 \cdot 10^{-4}$ m/s. The cross sections at $y = 0.07$ m and $y = 0.20$ m have significantly lower values of *Q/Re*. At higher Reynolds numbers, the local maxima near the midheight of the vessel do not exist and the peaks that are near the top and bottom of the tank at $Re = 20$ shift toward the midheight of the tank. At $Re = 200$, the global maximum of *Q/Re* is $8.1 \cdot 10^{-4}$ m/s at $y = 0.22$ m, with a slightly lower peak of $8.0 \cdot 10^{-4}$ m/s located near $y = 0.14$ m. The global maximum of *Q/Re* increases monotonically with increasing

Reynolds number, but this statement is not necessarily true for arbitrary horizontal cross sections within the vessel. A Lagrangian analysis of mixing behavior in this system at different Reynolds numbers will be the focus of a future communication and details concerning the mechanism of mixing in this system will be presented.

### *Deformation*

As an example of a physically relevant quantity that can be extracted from the simulation results but would be difficult to measure experimentally, the magnitude, $\xi$, of the rate of deformation tensor is computed along the vertical plane aligned with an impeller blade. The value of $\xi$ represents an upper bound for the local rate of generation of intermaterial area (Ottino, 1982). Since the local spatial derivatives of the velocity field are what determine the stretching, folding, and reorientation of fluid elements as they visit different locations in the flow, knowledge of the velocity gradients at different locations within the flow allows us to determine which regions have the greatest potential for mixing. Calculation of $\xi$ is also important because biofilm removal and cleaning both re-

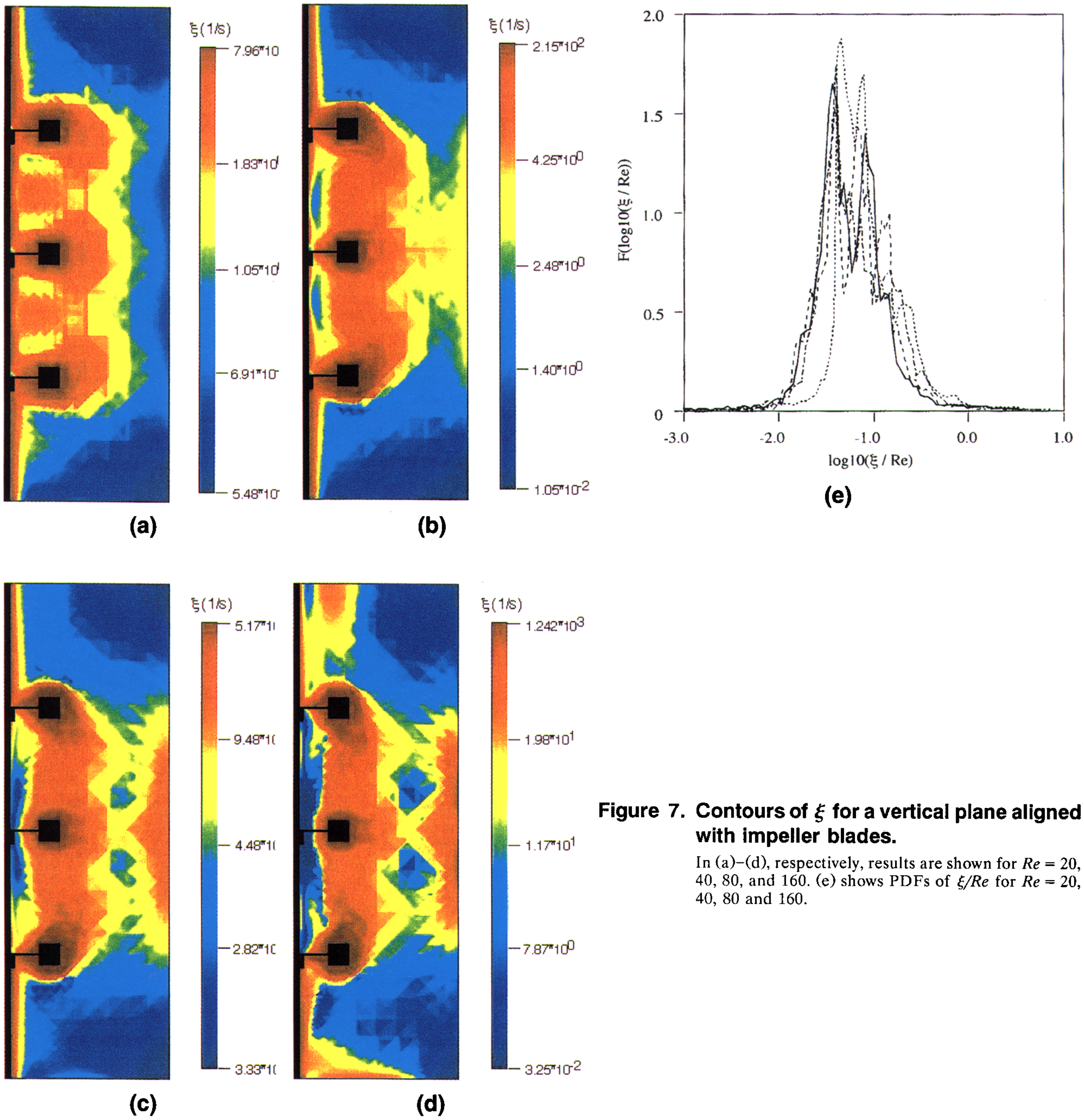

**Figure 7. Contours of $\xi$ for a vertical plane aligned with impeller blades.**

In (a)–(d), respectively, results are shown for $Re = 20$, 40, 80, and 160. (e) shows PDFs of $\xi/Re$ for $Re = 20$, 40, 80 and 160.

quire exceeding some minimum value of $\xi$. On the other hand, local regions of high $\xi$ could lead to excessive rates of cell damage and death in a bioreactor.

Figures 7a–7d show contour plots for $Re = 20$, 40, 80, and 160, respectively, for the vertical plane aligned with one of the impeller blades. In order to generate each contour plot, the points were sorted in order of increasing value of $\xi$, and the points with the lowest values of $\xi$ are plotted in dark blue, followed by light blue, green, yellow, orange, and red, which corresponds to points with the highest values of $\xi$. Color ranges are chosen so that each of the 64 colors used in the pictures represents approximately the same number of points. This method of coloring for the deformation magnitude plots is chosen because equal-sized bins result in contour plots that are difficult to analyze visually, since the values of $\xi$ span a large range and are distributed nonuniformly. The contour plot of $\xi$ for $Re = 20$ is shown in Figure 7a. The maximum value of $\xi$ along this plane is $7.96 \cdot 10^1$ s$^{-1}$, and the highest values of $\xi$ exist near the shaft and near the impeller blades. Small regions of high $\xi$ also exist between the impellers, but low magnitudes of deformation are evident throughout the rest of the cross section. At $Re = 40$ (Figure 7b), the maximum value of $\xi$ is $2.15 \cdot 10^2$ s$^{-1}$ and the structure of the contour plot is somewhat different than for $Re = 20$. Now, two regions of low $\xi$ exist near the shaft between the impellers, and a broad band of higher values of $\xi$ is now located near the tank wall. The plot for $Re = 80$ (Figure 7c) appears similar to that for $Re = 40$, except that now the band of high $\xi$ values near the vessel wall is more pronounced. The contour plots of $\xi$ have been quite symmetric with respect to the midheight of the tank for $Re = 20$, 40, and 80, but such symmetry does not exist for $Re = 160$ (Figure 7d). For this flow condition, the contour plot looks similar to that for $Re = 80$ (cf. Figure 7c), but regions of high $\xi$ exist near the bottom of the tank and near the top of the vessel close to the shaft for $Re = 160$. These four contour plots have qualitatively shown that for all flow conditions considered, significant spatial heterogeneity exists with regard to the magnitude of the deformation tensor for a vertical plane aligned with the impeller blades. The contour plots for the planes not aligned with the impeller blades are quite similar to those shown in Figure 7.

In order to quantitatively illustrate the differences in the magnitude of deformation at different Reynolds numbers for the vertical plane aligned with one of the impeller blades, the probability density functions (PDFs) for $\xi/Re$ are constructed according to Eq. 5:

$$F(\log_{10}(\xi/Re)) = \frac{1}{N}\frac{dN(\log_{10}(\xi/Re))}{d(\log_{10}(\xi/Re))}. \qquad (5)$$

The variable $\xi/Re$ is used because the magnitude of deformation increases with increasing Reynolds number and this normalization facilitates comparison of the PDFs for different Reynolds numbers. Here, $N = 75{,}000$ is the number of points along the vertical cross section and $dN(\log_{10}(\xi/Re))$ is the number of points that have values between $(\log_{10}(\xi/Re))$ and $(\log_{10}(\xi/Re)) + d(\log_{10}(\xi/Re))$. Figure 7e shows the resulting PDFs for $Re = 20$, 40, 80, and 160. In all cases, the distributions are quite broad and span several decades. For all four of these flow conditions, the distributions possess peaks near $\log_{10}(\xi/Re) = -1.0$ and $-1.5$; however, the PDFs tend to shift toward higher values with increasing $Re$. This observation indicates that overall, the magnitude of the deformation tensor increases nonlinearly with increasing Reynolds number.

## Discussion

Laminar flow and mixing in a stirred tank equipped with three Rushton turbines were investigated both computationally and experimentally. Ten Reynolds numbers between 20 and 200 were investigated and an unstructured mesh containing approximately 2 million tetrahedra was used. Using the ORCA software suite, geometry modeling, mesh generation, flow-field solution, and analysis can be performed within 24 h. This time frame indicates that CFD is now a mature tool for the analysis of geometrically complex, industrially relevant mixing devices. The CFD simulations agree very well with PIV data for bulk-flow patterns at several different agitation rates. Further, the sizes and locations of poor-mixing regions in computed Poincaré sections agree very well with results of PLIF experiments. Analysis of computed velocity fields indicated that significant spatial heterogeneity exists with regard to the magnitude of the deformation tensor. This work has shown that it is possible to use CFD to rapidly and accurately obtain large amounts of quantitative data concerning flow fields in complex industrial devices. This information will be used as a foundation for future communications that will involve a detailed Lagrangian analysis of mixing performance in the three-Rushton-turbine stirred tank.

## Literature Cited

Aiba, S., "Flow Patterns of Liquid in Agitated Vessels," *AIChE J.*, **4**, 485 (1958).

Ali, F., and M. Menzinger, "Stirring Effects and Phase-Dependent Inhomogeneity in Chemical Oscillations: The Belousov-Zhabotinsky Reaction in a CSTIR," *J. Phys. Chem. A*, **101**, 2304 (1997).

Alvarez, M. M., T. Shinbrot, J. M. Zalc, and F. J. Muzzio, "The Mechanisms of Chaotic Mixing in Stirred Tanks," *Science* (2000).

Ando, K., E. Obata, K. Ikeda, and T. Fukuda, "Mixing Time of Liquid in Horizontal Stirred Vessels with Multiple Impellers," *Can. J. Chem. Eng.*, **68**, 278 (1990).

Bakker, A., K. J. Myers, R. W. Ward, and C. K. Lee, "The Laminar and Turbulent Flow Patterns of a Pitched Blade Turbine," *Trans. Inst. Chem. Eng.*, **74A**, 485 (1996).

Biggs, R. D., "Mixing Rates in Stirred Tanks," *AIChE J.*, **9**, 636 (1963).

Bourne, J. R., and S. Yu, "Investigation of Micromixing in Stirred Tank Reactors Using Parallel Reactions," *Ind. Eng. Chem. Res.*, **33**, 41 (1994).

Cherry, R. S., and E. T. Papoutsakis, "Physical Mechanisms of Cell Damage in Microcarrier Cell Culture Bioreactors," *Biotechnol. Bioeng.*, **32**, 1001 (1988).

Croughan, M. S., J. Hamel, and D. I. Wang, "Hydrodynamic Effects on Animal Cells Grown in Microcarrier Cultures," *Biotechnol. Bioeng.*, **34**, 130 (1987).

Cui, Y. Q., R. G. van der Lans, H. J. Noorman, and K. Ch. Luyben, "Compartment Mixing Model for Stirred Reactors with Multiple Impellers," *Trans. Inst. Chem. Eng.*, **74**, 261 (1996).

Desouza, A., and R. W. Pike, "Fluid Dynamics and Flow Patterns in Stirred Tanks with a Turbine Impeller," *Can. J. Chem. Eng.*, **50**, 15 (1972).

Distelhoff, M. F. W., A. J. Marquis, J. M. Nouri, and J. H. Whitelaw, "Scalar Mixing Measurements in Batch Operated Stirred Tanks," *Can. J. Chem. Eng.*, **75**, 641 (1997).

Godfrey, J. C., "Static Mixers," *Mixing in the Process Industries*, N. Harnby, M. F. Edwards, and A. W. Niewnow, eds., Butterworth-Heinemann, Woburn, MA (1992).

Harvey, A. D., and S. E. Rogers, "Steady and Unsteady Computation of Impeller-Stirred Reactors," *AIChE J.*, **42**, 2701 (1996).

Harvey, A. D., D. H. West, and N. B. Tufillaro, "Evaluation of Laminar Mixing in Stirred Tanks Using a Discrete-Time Particle Mapping Procedure," *Chem. Eng. Sci.*, **55**, 667 (2000).

Hayes, R. E., A. Afacan, B. Boulanger, and P. A. Tanguy, "Experimental Study of Reactive Mixing in a Laminar Flow Batch Reactor," *Trans. Inst. Chem. Eng.*, **76**, 73 (1998).

Holden, P. J., M. Wang, R. Mann, F. J. Dickin, and R. B. Edwards, "Imaging Stirred-Vessel Macromixing Using Electrical Resistance Tomography," *AIChE J.*, **44**, 780 (1998).

Hudcova, V., V. Machon, and A. W. Nienow, "Gas-Liquid Dispersion with Dual Rushton Turbine Impellers," *Biotechnol. Bioeng.*, **34**, 617 (1989).

Jahoda, M., and V. Machon, "Homogenization of Liquids in Tanks Stirred by Multiple Impellers," *Chem. Eng. Technol.*, **17**, 95 (1994).

LaFontaine, R. F., and I. C. Shepherd, "Particle Image Velocimetry Applied to a Stirred Vessel," *Exp. Therm. Fluid Sci.*, **12**, 256 (1996).

Lamberto, D. J., M. M. Alvarez, and F. J. Muzzio, "Experimental and Computational Investigation of the Laminar Flow Structure in a Stirred Tank," *Chem. Eng. Sci.*, **54**, 919 (1999).

Montes, F. J., M. A. Galan, and R. L. Cerro, "Mass Transfer from Oscillating Bubbles in Bioreactors," *Chem. Eng. Sci.*, **54**, 3127 (1999).

Norwood, K. W., and A. B. Metzner, "Flow Patterns and Mixing Rates in Agitated Vessels," *AIChE J.*, **6**, 432 (1960).

O'Connell, F. P., and D. E. Mack, "Simple Turbines in Fully Baffled Tanks," *Chem. Eng. Prog.*, **46**, 358 (1950).

Ottino, J. M., "Description of Mixing with Diffusion and Reaction in Terms of the Concept of Material Surfaces," *J. Fluid Mech.*, **114**, 83 (1982).

Ranade, V. V., "An Efficient Computational Model for Simulating Flow in Stirred Vessels: A Case of Rushton Turbine," *Chem. Eng. Sci.*, **52**, 4473 (1997).

Rushton, J. H., E. W. Costich, and H. J. Everett, "Power Characteristics of Mixing Impellers: Part I," *Chem. Eng. Prog.*, **46**, 395 (1950).

Saravanan, K., A. W. Patwardhan, and J. B. Joshi, "Critical Impeller Speed for Solid Suspension in Gas Inducing Type Mechanically Agitated Contactors," *Can. J. Chem. Eng.*, **75**, 664 (1997).

Smith, F. G., "A Model of Transient Mixing in a Stirred Tank," *Chem. Eng. Sci.*, **52**, 1459 (1997).

Wichterle, K., "Drop Breakup by Impellers," *Chem. Eng. Sci.*, **50**, 3581 (1995).

Xu, G. J., Y. M. Li, Z. Z. Hou, L. F. Feng, and K. Wang, "Gas-Liquid Dispersion and Mixing Characteristics and Heat Transfer in a Stirred Vessel," *Can. J. Chem. Eng.*, **75**, 299 (1997).

Zalc, J. M., and F. J. Muzzio, "Parallel-Competitive Reactions in a Two-Dimensional Chaotic Flow," *Chem. Eng. Sci.*, **54**, 1053 (1999).

*Manuscript received March 13, 2000.*